

RESEARCH

Open Access



Low-radiation dose XRF excited by MeV protons for cultural heritage samples

Yoshiyuki Oguri^{1*}, Hitoshi Fukuda², Jun Hasegawa³ and Naoto Hagura⁴

Abstract

In this work, we tested a setup of X-ray fluorescence (XRF) excited by proton-induced quasi-monochromatic X-rays (proton-induced XRF (PIXRF)) as a low-radiation dose analytical technique for precious cultural heritage samples. The low-dose performance of the PIXRF is experimentally assessed in comparison with the performance of a conventional XRF. For this assessment, we prepared test samples, which simulated original Japanese paintings with copper-bearing pigments. By introducing a figure-of-merit, the PIXRF is found to potentially give a better performance in terms of the radiation dose to the sample and the limit of detection, albeit the degraded multi-elemental analytical capability. PIXRF can be a cost-effective method to perform low dose measurements of precious samples, if introduced in an existing PIXE facility.

Keywords XRF, PIXE, Proton-induced X-ray, Radiation damage, Limit of detection, Radiation dose, Japanese painting, Pigment, Copper, Cobalt

Introduction

In high-sensitivity elemental analysis of historical heritage samples, X-ray analytical techniques, such as particle-induced X-ray emission (PIXE) and X-ray fluorescence (XRF), are generally regarded as non-destructive. Particularly, benchtop and handheld XRF devices are widely used in this field of research.

However, in PIXE analysis, the MeV protons directed to the sample induce not only the desired X-ray emission, but also a finite undesired radiation damage that can develop into detectable macroscopic effects, such

as discoloration [1] and increased brittleness [2], in the irradiated sample. Considering this, a guideline has been provided for cultural heritage sample characterization by ion beam analysis, including PIXE [3].

With regard to the linear energy transfer of probe beams, XRF is less harmful to samples than PIXE. Nevertheless, a very high dose of primary X-rays, such as few-kW of radiative power for several minutes or more, can induce severe effects, e.g., a change of color in the samples [4], which is totally unacceptable for heritage samples. For inorganic materials in heritage samples, there exist a few studies in which threshold doses are given in Gy (J/kg) units [5]. In addition, damage in organic materials depends on case-by-case scenarios, and the X-ray dose data in Gy are usually not available. Instead, the X-ray dose data in many studies are given only in the operational parameters of the X-ray tube, such as the “tube voltage \times anode current \times time” [4]. Thus a “safe” dose has yet to be well defined. Moreover, damages due to radiation are considered cumulative [6]. Accordingly, the radiation dose by cultural heritage analysis should be determined according to the “As Low As Reasonably Achievable (ALARA)” principle [7].

*Correspondence:

Yoshiyuki Oguri
ysyokgr@gmail.com

¹ NAT Research Center, NAT Corporation, 3129-45, Hibara Muramatsu, Tokai-Mura, Naka-Gun, Ibaraki 319-1112, Japan

² Safety and Radiation Management Division, Open Facility Center, Tokyo Institute of Technology, 2-12-1, Ookayama, Meguro-Ku, Tokyo 152-8550, Japan

³ Laboratory for Zero-Carbon Energy, Institute of Innovative Research, Tokyo Institute of Technology, 2-12-1, Ookayama, Meguro-Ku, Tokyo 152-8550, Japan

⁴ Department of Nuclear Safety Engineering, Tokyo City University, 1-28-1, Tamazutsumi, Setagaya-Ku, Tokyo 158-8557, Japan

Most conventional XRF systems have a continuous primary X-ray energy spectrum (Fig. 1a). In contrast, the element of interest has specific absorption characteristics represented by the absorption edge. Primary photons with energies below the edge have no contribution. Similarly, photons with energies much higher than the edge cannot produce KX-ray emission efficiently. Nevertheless, these components can induce unnecessary radiation damage to the sample. Accordingly, these components should be minimized to maximize the XRF yield per radiation dose to the sample. Synchrotron radiation and X-ray lasers are usually not easily accessible, and their performances are excessive for simple XRF applications. Hence, a more easily accessible inexpensive method is desired for the scientific study of historical heritage samples.

In contrast to the electron-induced X-ray emission in X-ray tubes, if a single-element target is irradiated by MeV protons, quasi-monochromatic X-rays consisting mostly of the characteristic X-rays of the element can efficiently be produced (Fig. 1b). These quasi-monochromatic X-rays can be used as primary X-rays for XRF [8–25]. One advantage of this method over employing an X-ray tube coupled to a secondary anode is its better

spectral quality [8]. On the other hand, even if the whole system is integrated as an XRF device, it cannot even be desktop-sized, because a large megavolt accelerator is required to produce the primary proton beam. The weight may exceed 1 ton, and the machine can be portable only by using a vehicle. Vacuum is essential for production, transport, and irradiation of the proton beam. However, once the primary X-ray is emitted through a vacuum window, both the sample and the detector can be in an atmospheric pressure environment.

Proton-induced XRF (PIXRF) mentioned above has been tested for analysis of many kinds of samples, including cultural heritage ones [9, 13, 14, 18–23]. Low-background and high element selective capabilities have been emphasized in many studies. Authors have demonstrated the low-dose performance of PIXRF employing an in-vivo plant measurement [24, 25]. In these experiments, the radiation doses of the primary X-ray were low enough to keep the plant sample alive during the measurement. This technique can also be applied to low-dose XRF analysis of precious historical samples. However, a quantitative comparative experiment on the radiation dose between PIXRF and conventional XRF has not yet been implemented.

Restoration and conservation of paint layers of artefacts are an essential task in many museums. The vast majority of the pigments are inorganic, whereas the support, binding media, and eventual varnish are organic. In addition, even the inorganic pigments can be reactive and can produce degradation products due to interaction with impurities and environment [26]. Hence, considering the importance of heritage conservation, paint layers consisting of inorganic pigments and organic binders were selected as the object of our study. In Japan, copper (Cu, $Z=29$)-bearing natural minerals are traditionally used as blue-green pigments for artefacts [27–30]. In the seventeenth century, however, imported cobalt (Co, $Z=27$)-based blue pigments started to be used in some paintings as a substitute for the traditional Cu-based pigment [31]. The mixed use of both these pigments has also been identified in some paintings [32, 33]. Therefore, not only Cu quantification, but also selective Co measurement in samples containing Cu as a major element are important from the viewpoint of the history of trades and cultural exchange between the East and the West in the early modern period.

This study aims to present the radiation dose due to the abovementioned PIXRF technique in the analysis of precious cultural heritage samples, in which the damage caused by the radiation dose should be minimized as much as possible. As an example, we focus herein on Cu and Co analysis in inorganic blue pigments used for the historical Japanese painting described earlier. The

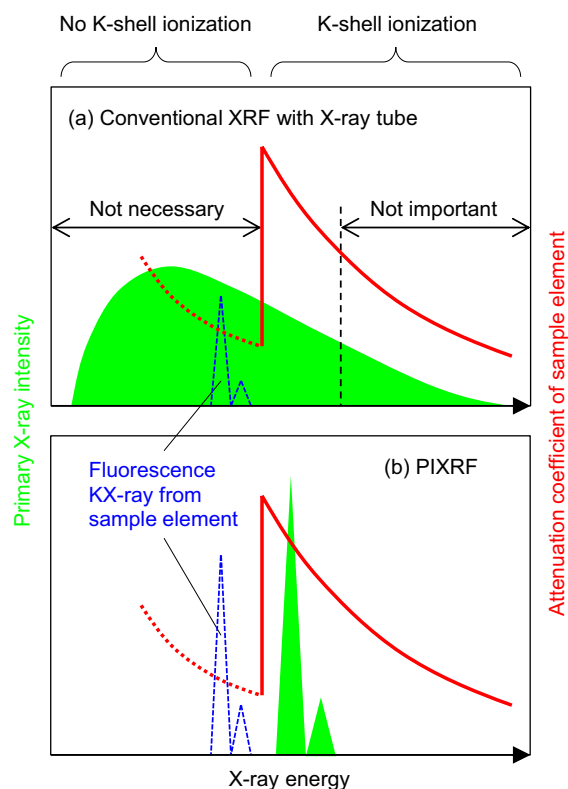


Fig. 1 Energy spectrum of the primary X-rays and the K-absorption edge structure of the sample element in **a** conventional XRF and **b** PIXRF

experimental results for the simple standard and simulated historical samples are presented. The selective measurement of Co from Cu in the sample is also examined. The results are then used to quantitatively evaluate the limit of detection (LOD) for Cu and the radiation dose received by the sample due to the measurement. The trade-off between the LOD as an analytical capability and the radiation dose to the sample is discussed in terms of a figure-of-merit.

Materials and methods

Proton-induced X-ray source

Figure 2 illustrates the PIXRF experiment setup, which is a palm-sized unit, where the distance from the target to the sample is only 14 cm and can easily be attached to an accelerator beam line.

A 2.5 MeV proton beam was delivered by an electrostatic tandem accelerator at Tokyo Tech. After passing through a $\phi 3$ mm aperture, the protons impinged on a single-element target in a compact ($3.4 \times 3.4 \times 3.4$ cm³) vacuum chamber. The chamber was electrically isolated, such that the proton beam current on the target could be measured. Two different kinds of target could be irradiated at the center of the chamber. The beam size on the target was monitored by a quartz scintillator at the target position and adjusted to $\phi 2$ – 3 mm using a magnetic

quadrupole. The proton beam current on the target was ≈ 200 – 300 nA.

The K-absorption edge energy of Cu is 8.98 keV. We selected germanium (Ge, $Z=32$) as the target element, which emits 9.87 keV K_{α} X-rays, to efficiently induce the K-shell ionization of Cu. We used a commercially available Ge disk (7 mm diameter \times 3 mm height, 99.999%, Takachiho Metal Co., Ltd.) as the proton beam target. For the Co measurement (K-shell absorption edge at 7.71 keV), a Cu target was used to induce the Cu - K_{α} X-rays (8.04 keV) as the primary photons. The proton-induced X-rays were emitted through a 50 μ m-thick Mylar window to the atmosphere. To simplify the design of the sample irradiation port and to obtain a well-defined beam spot size of primary X-rays, we used a polycapillary X-ray half lens with a focal length of 45 mm (Unisantis Europe GmbH) to focus the X-rays onto the sample. The focal spot size was $\phi 250$ μ m (spot area = 0.049 mm²) [24]. However, this spot size is approximately 10 times larger than those of the benchtop micro-XRF instruments [34]. Therefore, if the aforementioned system is used practically, only plain and large areas can be analyzed, as in the case of handheld XRF devices; it would not be possible to analyze, e.g., cross-sections of paintings with many paint layers.

Comparison of the performances between the PIXRF setup presented above and, e.g., a commercially available benchtop device is very complex, because many factors including the X-ray source and X-ray detector, are different. Therefore, we built an equivalent of the PIXRF setup employing an X-ray tube (Mini-X, AMPTEK, Inc.) for comparison. The anode voltage and current were 20 kV and 100 μ A, respectively. A 15 μ m-thick aluminum foil was attached to the window of the X-ray tube to manipulate the energy spectrum, such that its peak could be exactly at the absorption edge energy of Cu. In this setup, the X-rays were also focused onto the sample by the X-ray lens in the same manner as in the PIXRF experiment.

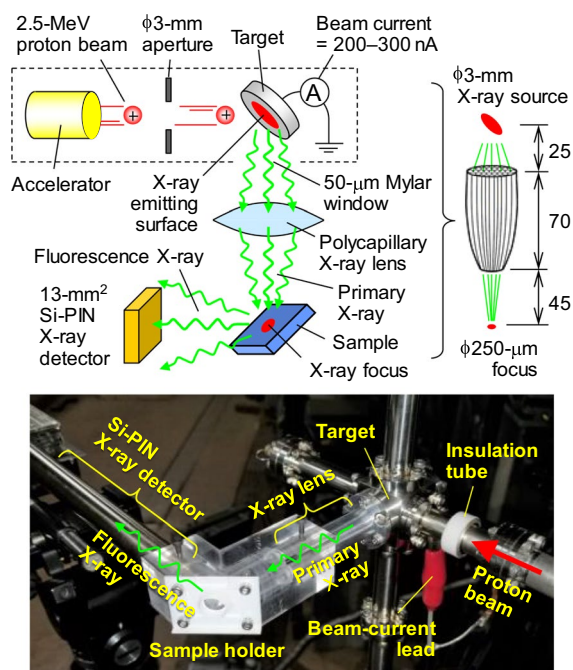


Fig. 2 Schematic illustration (upper) and photograph (lower) of the PIXRF setup. For a comparative conventional XRF measurement, the part surrounded by the dashed lines in the illustration was changed to the X-ray tube

Detector system

The fluorescence X-rays from the sample were detected by a Si-PIN semiconductor detector (XR-100CR, AMPTEK, Inc.). The detector size was 13 mm² (sensitive area) \times 0.5 mm (thickness). The Be-window thickness was 25.4 μ m. The distance between the Be-window and the sample was 11 mm. The signal from the detector amplifier was processed by a 2048-channel pulse height analyzer. The spectrum measurement time per sample ranged from 30 min to 2 h depending on the samples. The total primary X-ray fluence to the sample was determined from the total proton charge measured by a current integrator (ORTEC 439) connected to the target.

For the absolute measurement of the energy spectra of the primary X-rays, the 90° attachment with the sample holder in Fig. 2 was removed, and the Si-PIN detector was put exactly at the focal position of the X-ray lens. In this measurement, the X-ray intensity was decreased by a factor of $\approx 10^2$ by reducing the proton beam current to prevent the X-ray pulse pile-ups.

Sample preparation

In East Asian paintings, animal glue is used as common base binding material for inorganic pigments. Glues are also used, mixed with alum, as a sizing agent (dosa) for preparing the paper before painting. As another binding material, starch paste has been used mostly for lining and mounting [35, 36]. Although all these organic materials can be affected by incident X-ray radiation, the present study focuses on the damage to the paint layer, which is commonly regarded as a mixture of mineral pigment and animal glue.


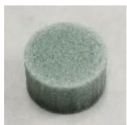

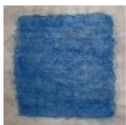
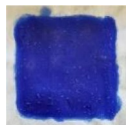

Table 1 summarizes the details of the samples prepared in this study. Thick samples with low Cu concentrations were prepared (samples #1 to #3) to evaluate the LOD of the system. Copper(II) sulfate pentahydrate ($\text{CuSO}_4 \cdot 5\text{H}_2\text{O}$, FUJIFILM Wako Pure Chemical Corp.) was used as the Cu compound. Gelatin ($\text{C}_{65}\text{H}_{102}\text{N}_{18}\text{O}_{21}$), which simulated the animal glue (collagen) used in traditional Japanese paintings, was used as the base binder material [37]. A small amount of $\text{CuSO}_4 \cdot 5\text{H}_2\text{O}$ was dissolved to an aqueous gelatin (FUJIFILM Wako Pure Chemical Corp.) solution. After completely drying this solution in a mortar, the residue was crushed by a pestle and filtered by a 200 μm stainless steel mesh.

Subsequently, 1 g powder was pressed into a cylindrical pellet using a hydraulic press with 2 ton/ cm^2 pressure. The pellet size was 12 mm in diameter and ≈ 7 mm in height. We prepared pellets with Cu concentrations (w/w) of 0, 1000, and 10,000 ppm.

To demonstrate the applicability of the present setup to the artefact samples, we prepared samples simulating actual paintings. Japanese hemp paper (thickness = 4.5 mg/ cm^2 , Ohnao Co., Ltd.) was used as the support material. The commercially available powder of the azurite ($\text{Cu}_3(\text{CO}_3)_2(\text{OH})_2$, *Iwa-gunjo* in Japanese) blue pigment (#731, Nakagawa gofun enogu Co., Ltd.) and the same mass of gelatin were dissolved in warm water. The hemp paper was then painted with this pigment solution using a brush (Sample #4). Similarly, a sample with smalt (fine powder of $\text{SiO}_2 \cdot \text{K}_2\text{O} \cdot \text{CoO}$ glass, *Hana-konjo* in Japanese) (#860, Nakagawa gofun enogu Co., Ltd.) was prepared for the Co measurement (Sample #5). The CoO content (w/w) was assumed to be 10% [38]. The mass thicknesses or areal densities of azurite and smalt paint, including glue on the paper after drying, were 6.1 mg/ cm^2 and 42 mg/ cm^2 , respectively. These thicknesses were determined such that the areal concentrations of Cu and Co were equal (1.7 mg/ cm^2).

A sample with a mixture of azurite and smalt was also prepared to demonstrate the element-selection capability (Sample #6). The mixing ratio for this sample was 1:1 in pigment-weight basis. The mass thickness of the mixed paint including glue on the paper after drying was 16 mg/ cm^2 . The corresponding areal densities of Cu and Co on the hemp paper support were 2.2 mg/ cm^2 and 0.31 mg/ cm^2 , respectively.

Table 1 Samples prepared in this study

	Thick standard sample for LOD evaluation			Simulated cultural heritage sample		
Sample number	#1	#2	#3	#4	#5	#6
						
Compound or pigment	Copper(II) sulfate pentahydrate ($\text{CuSO}_4 \cdot 5\text{H}_2\text{O}$)			Azurite ($\text{Cu}_3(\text{CO}_3)_2(\text{OH})_2$)	Smalt ($\text{SiO}_2 \cdot \text{K}_2\text{O} \cdot \text{CoO}$)	Azurite + smalt
Base binding medium	Gelatin ($\text{C}_{65}\text{H}_{102}\text{N}_{18}\text{O}_{21}$)					
Support material	(None)			4.5 mg/ cm^2 -thick Japanese hemp paper		
Preparation method	Homogenization and pelletization			Painting on paper support and drying		
Element of interest	Cu			Cu	Co	Cu and Co
Mass concentration	0 ppm	1000 ppm	10,000 ppm	28% ^a	3.9% ^a	Cu 14% ^a Co 2.0% ^a
Thickness	≈ 7 mm (cylindrical pellet height)			140 μm^b	340 μm^b	190 μm^b

^a Concentration in the pigment-glue mixture after drying

^b Measured whole thicknesses of the paper permeated with the pigment solution after drying

The geometrical thicknesses of the painted layers of the simulated cultural samples (samples #4 to #6) can hardly be measured due to permeation of the pigment solution into the paper support. Therefore, Table 1 demonstrates the whole thicknesses of the paper permeated with the pigment solution (after drying) measured with a micrometer caliper.

Results and discussion

Primary X-ray spectra

Figure 3a shows the measured energy spectrum of the primary X-rays produced by irradiating the Ge target with protons. The mass energy absorption coefficient of Cu as a function of the X-ray energy [39] is plotted, as well. As expected, only the Ge-KX-rays are clearly visible. Almost no continuous emission caused by Bremsstrahlung, which is the main component of emission from X-ray tubes, can be found. The Ge-K α X-ray energy was slightly higher than the absorption edge energy of Cu. Therefore, the XRF yield was expected to be nearly maximum. Figure 3b depicts the spectrum for the Cu target

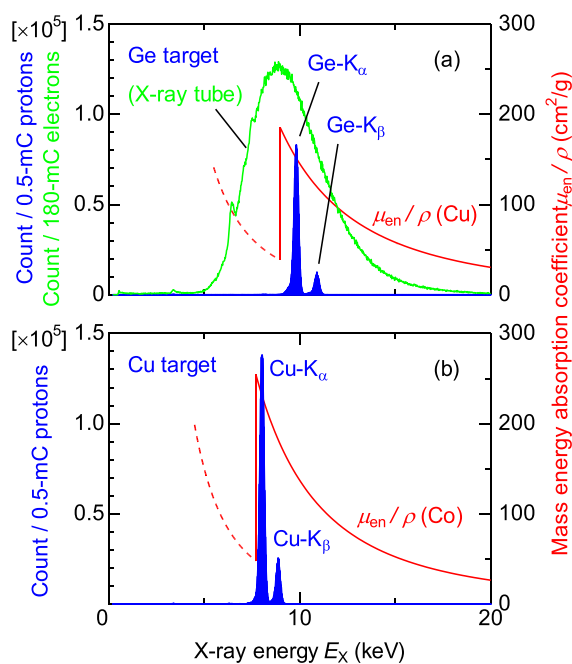


Fig. 3 **a** Measured energy spectra of the primary X-rays from the Ge target for PIXRF (blue) and the X-ray tube for conventional XRF (green). The absorption characteristics of Cu as the sample element were plotted as a function of the X-ray energy (red). **b** Measured energy spectra of the primary X-rays from the Cu target for PIXRF (blue). The absorption characteristics of Co as the sample element were plotted, as well (red). The proton and electron charges shown in the ordinates indicate the total charges (current \times time) of these particles impinging on the targets for PIXRF and the anode in the X-ray tube, respectively

for the Co measurement, where the Cu-KX-ray energy is well-suited for the Co K-shell excitation.

The measured energy spectrum of the X-rays from the X-ray tube is also plotted in Fig. 3a for comparison. Different from the proton-induced X-ray, the spectrum was continuous. Nevertheless, thanks to the anode voltage adjustment and the Al filter insertion, the spectrum peak could be tuned exactly at the absorption edge energy of Cu. Although the anode material of this tube was silver (Ag, $Z=47$), no Ag-KX-ray peak (K_α at 22.1 keV, K_β at 24.9 keV) was observed because the anode voltage was 20 kV.

LOD for Cu

Figure 4a–c show the PIXRF energy spectra measured for the thick targets with 0 ppm (Blank, background) (Sample #1), 1000 ppm (Sample #2), and 10,000 ppm Cu (Sample #3), respectively, using the Ge primary target. Together with the peaks caused by the scattering of the primary Ge-KX-rays, the peaks of the Cu-K emissions are clearly visible in Fig. 4b, c. The peak at ≈ 3.4 keV was caused by the electronic noise that appeared, even when the primary X-ray was off. This peak unfortunately overlapped the potassium (K) KX-ray peaks observed to be caused by K in gelatin as a minor element. The background continuum in Fig. 4a was very weak. From these spectra, the net count N_{net} of the Cu-K α X-ray could be evaluated and plotted as a function of the Cu concentration C_{Cu} in Fig. 5. In the upper graph, the vertical error bars indicate statistical errors evaluated by N_{net} and background counts N_{BG} under the peaks. The widths of the horizontal error bars were determined by the errors due to the multiple dilution process of the $\text{CuSO}_4 \cdot 5\text{H}_2\text{O}$ solution during the standard sample preparation. The LOD for Cu in the mass concentration unit was calculated as follows [40]:

$$\text{LOD}_{\text{Cu}} = \frac{3\sqrt{N_{\text{BG}}C_{\text{Cu}}}}{N_{\text{net}}}, \quad (1)$$

where $\sqrt{N_{\text{BG}}}$ represents the standard deviation of N_{BG} . The ratio $N_{\text{net}}/C_{\text{Cu}}$ represents the sensitivity that is equal to the calibration line slope in Fig. 5, which was determined by a linear regression considering errors in both axes. By substituting the values of the calibration line slope above, we obtained $\text{LOD}_{\text{Cu}}=80$ ppm, while N_{BG} was obtained from the measured spectra in Fig. 4. This LOD value was much higher than that of commercially-available conventional XRF devices [41, 42]. This result can be explained by the poorer signal-to noise ratio due to the lower primary X-ray intensity used.

Figure 6a–c show the conventional XRF spectra for the 0-ppm (Blank, background) (Sample #1), 1000-ppm (Sample #2), and 10,000 ppm Cu (Sample #3) samples,

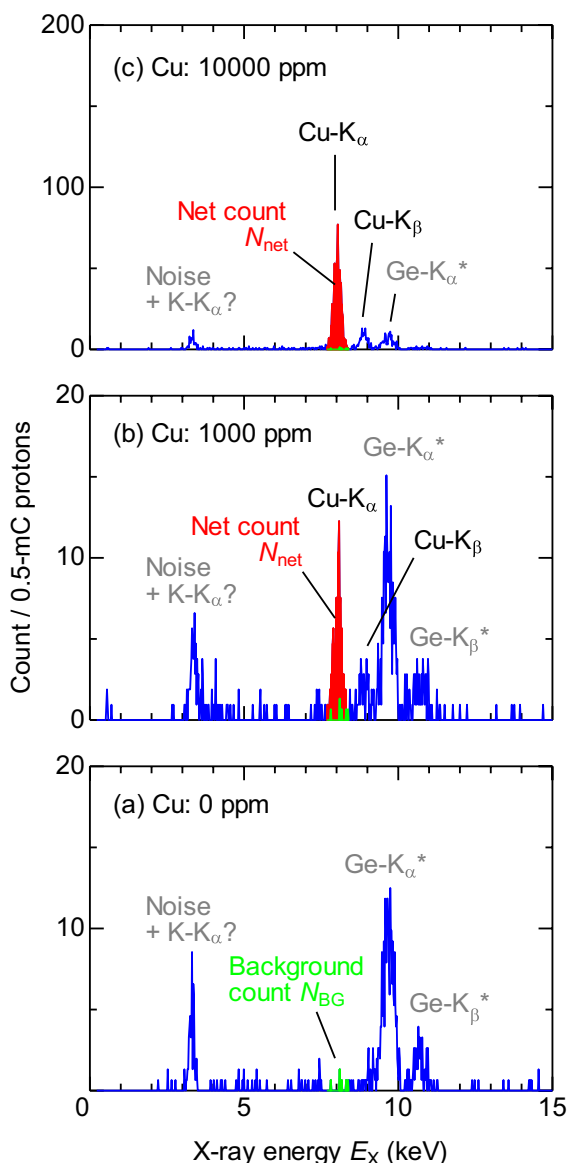


Fig. 4 PIXRF energy spectra measured for the thick samples with **a** 0-ppm (blank) (Sample #1), **b** 1000-ppm (Sample #2) and **c** 10,000-ppm (Sample #3) Cu using the Ge target. The asterisks (*) indicate the peaks of the scattered primary photons

respectively, measured using the X-ray tube. In contrast to that for PIXRE, the spectrum suffered from a continuous background due to the primary X-ray scattering. Nevertheless, at least for this Cu concentration, the Cu-K_αX-ray yield was enough for the Cu quantification. Figure 7 illustrates the calibration line drawn in a similar manner to that in Fig. 5. From this graph, LOD=32 ppm, which is 2.5-times better than that of PIXRF. This result is attributed to the better statistical accuracy of the spectrum measurement caused by the

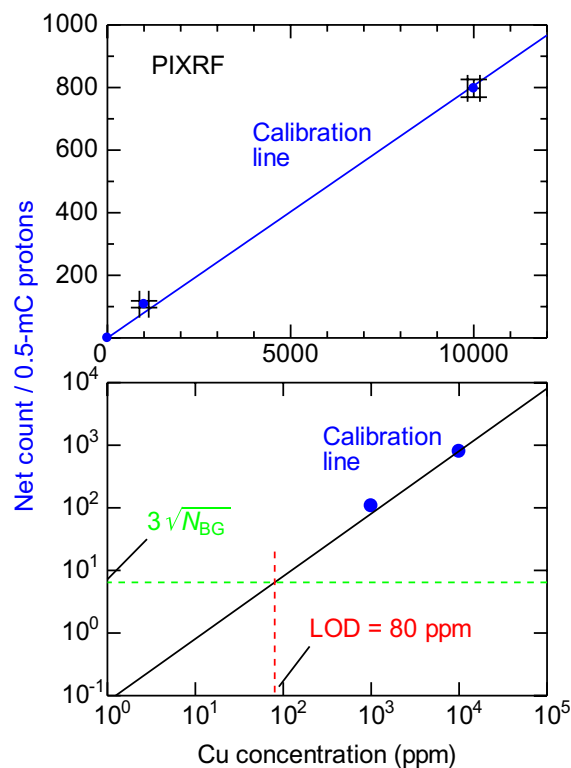


Fig. 5 Net yield of the Cu-K_αX-rays as a function of the Cu concentration (calibration line) for the PIXRF experiment in linear (upper) and logarithmic (lower) scales

higher intensity of the primary X-rays in the conventional XRF experiment.

Radiation dose to the samples

Considering the energy dependence of the fluence–dose relationship, the radiation dose to the sample surface was calculated as follows based on the measured energy spectrum:

$$D = \Phi \int_0^\infty E_X \frac{\mu_{en}(E_X)}{\rho} f(E_X) dE_X, \tag{2}$$

where Φ is the total incident X-ray fluence (=photons per area); ρ is the target mass density; and $\mu_{en}(E_X)$ is the energy absorption coefficient as a function of the photon energy E_X . The samples consisted of many element species; thus, this quantity was calculated as

$$\mu_{en}(E_X) = \rho \sum_i w_i \frac{\mu_{en}(E_X)}{\rho} \Big|_i, \tag{3}$$

where $\mu_{en}(E_X)/\rho|_i$ is the mass energy absorption coefficient [39] of the *i*th element, and w_i is the mass fraction of the *i*th element satisfying

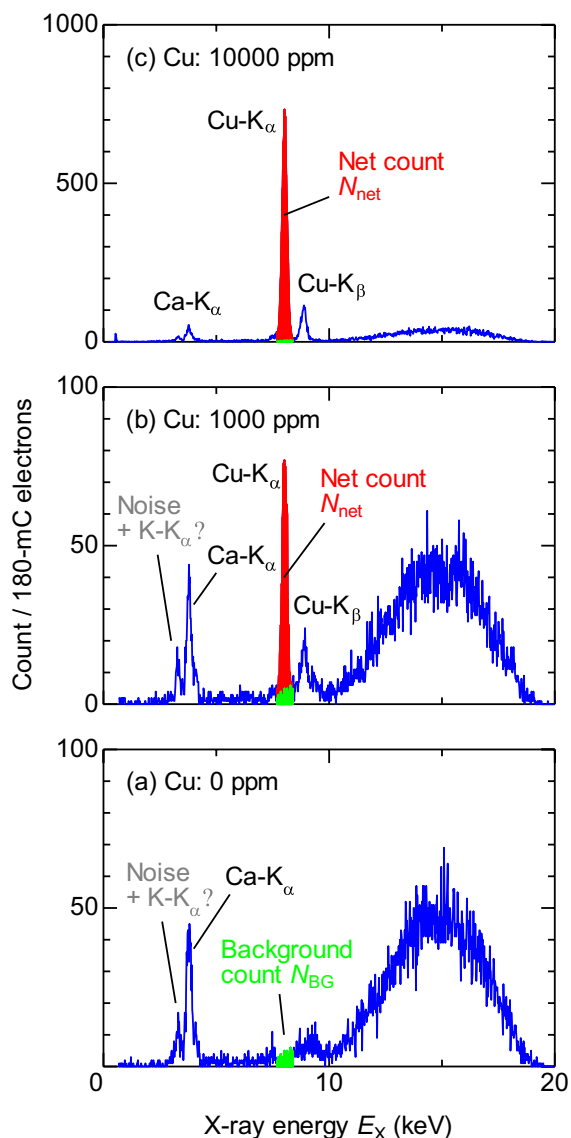


Fig. 6 Conventional XRF spectrum measured for the thick samples with **a** 0-ppm (blank) (Sample #1), **b** 1000-ppm (Sample #2) and **c** 10,000-ppm (Sample #3) Cu using the X-ray tube

$$\sum_i w_i = 1. \tag{4}$$

In Eq. (2), the $f(E_X)$ function is the energy spectrum of the incident X-rays fulfilling the normalization condition that

$$\int_0^\infty f(E_X) dE_X = 1. \tag{5}$$

We determined $f(E_X)$ under the condition above using the measured spectra in Fig. 3a and the detector efficiency curve published by the manufacturer [43]. Using

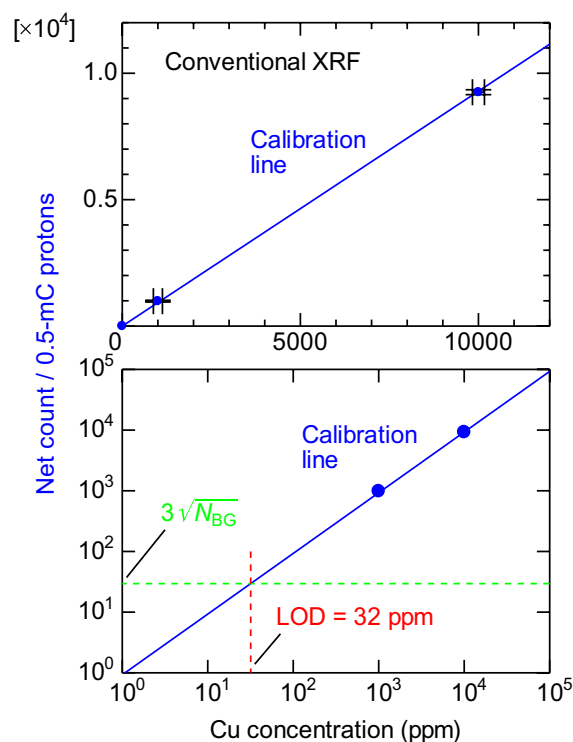


Fig. 7 Net yield of the Cu- K_α X-rays as a function of the Cu concentration (calibration line) for the conventional XRF measurement in linear (upper) and logarithmic (lower) scales

these formulas, we calculated the dose D in Gy (=J/kg) unit to the samples. Table 2 summarizes the result together with the LOD data for the PIXRF and conventional XRF experiments. In the present setup, the dose caused by PIXRF was 14 mGy, which was only $\approx 1/30$ of the dose by the conventional XRF (i.e., 430 mGy). This result can be explained by the spectral shape of the primary X-rays shown in Fig. 3a, where the photon energy was tuned to ionize the Cu K-shell.

The trade-off between the LOD and the radiation dose was considered based on the following simple calculation: N_{net} in Eq. (1) is proportional to the product of C_{Cu} and the number of incident primary X-ray photons I_X , whereas N_{BG} is proportional only to I_X , that is,

$$N_{\text{net}} \propto I_X C_{\text{Cu}}, \tag{6}$$

$$N_{\text{BG}} \propto I_X. \tag{7}$$

In contrast, the dose D is proportional not to I_X , but to the photon fluence Φ :

$$D \propto \Phi \propto \frac{I_X}{A}, \tag{8}$$

Table 2 Comparison of the observation area (*A*), detection limit of Cu (LOD_{Cu}), radiation dose (*D*) and figure-of-merit (FOM_D) performances among PIXRF, conventional XRF, and a commercially available handheld XRF device

Analytical method		<i>A</i> (mm ²)	LOD_{Cu} (ppm)	<i>D</i> (mGy)	FOM_D (mGy·mm ² ·ppm ²)
This study	PIXRF	0.049	80	14	4×10^3
	Conventional XRF		32	430	2×10^4
Commercially-available handheld XRF [42, 44]		25	5–7	670	$4\text{--}8 \times 10^4$

where *A* denotes the observation area equal to the primary X-ray spot area on the target. From Eqs. (6)–(8), LOD_{Cu} in Eq. (1) becomes

$$LOD_{Cu} \propto \frac{1}{\sqrt{DA}}, \text{ or } D \propto \frac{1}{A \times LOD_{Cu}^2}. \quad (9)$$

Thus, we can define the figure-of-merit FOM_D in terms of the radiation dose given as

$$FOM_D \equiv DA \times LOD_{Cu}^2, \text{ or } D = \frac{FOM_D}{A \times LOD_{Cu}^2}. \quad (10)$$

It follows that the radiation dose is proportional to FOM_D if $A \times LOD_{Cu}^2$ is the same. Therefore, a smaller FOM_D translates into better low-dose performance. Table 2 summarizes the data on LOD_{Cu} , *A*, *D*, and calculated FOM_D for the PIXRF and conventional XRF experiments. The FOM_D performance of PIXRF was approximately five times better (i.e., *D* was approximately five times lower) than that of the conventional XRF setup. It is noted that the experimental *D* value of the PIXRF was 30 times lower than that of the conventional XRF. However, if the primary X-ray fluence (X-ray intensity × time) for PIXRF was increased to ensure that the LOD_{Cu} values of both methods were equal, the dose by the PIXRF would have been only five times lower than that of conventional XRF.

For reference, we roughly estimated the FOM_D for a commercially available handheld XRF device, namely the DELTA family handheld XRF analyzer from OLYMPUS INNOV-X. For this calculation, the *A* (25 mm²) and LOD_{Cu} (5–7 ppm) values were obtained from the user manual [44] and brochure [42] of this product, respectively. The dose *D* was calculated from the data on these documents (dose rate = 20,000 mSv/h, measurement time = 2 min), assuming that 1 Sv was equivalent to 1 Gy. Table 2 also presents the calculated results and relevant data. Although a simple comparison is not appropriate, the FOM_D of PIXRF herein is lower than those of the equivalent conventional XRF and the commercial product, i.e., the low-dose performance of the PIXRF is better than the other techniques examined. In this work, the conventional XRF experiment showed a better FOM

performance than the commercial device. One possible reason for this is that the energy spectrum of the primary photons from the X-ray tube was tuned to efficiently induce Cu K-shell ionization (Fig. 3a).

In the actual painting sample analysis, not only organic binder materials, but also mineral-based pigment materials can be damaged by the incident X-ray. When the pigment particles are small, the low-energy secondary electrons from the Cu atoms, including Auger electrons, can give a high dose to the surrounding organic materials [45]. Hence, using Eq. (2), we re-examined the dose to the painted layer, where azurite and gelatin were mixed. Figure 8 plots the results as a function of the mixing ratio of azurite. In this figure, we adjusted the number of incident primary X-ray photons according to Eq. (9), such that the LOD_{Cu} of both analytical methods were equal (80 ppm). For both analytical methods, the dose was very sensitive to and increased with the increasing azurite content because the primary X-ray energy was tuned to Cu detection in azurite. For example, Fig. 8 reveals that the dose to Sample #4 is 15 times higher than that to the pure gelatin sample (Sample #1). Thus the low-dose performance of PIXRF shown in Table 2 was degraded when actual

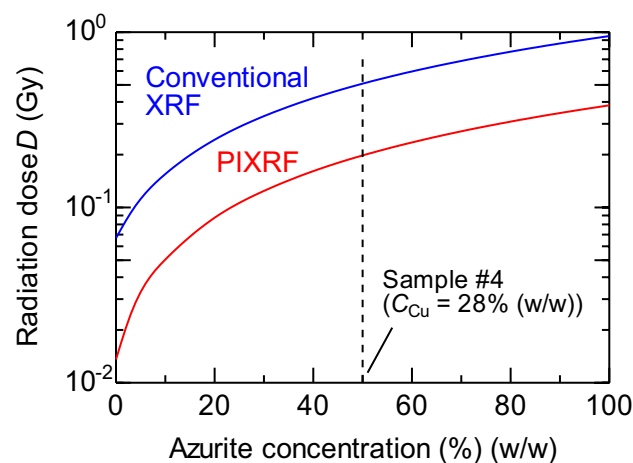


Fig. 8 Radiation dose to the azurite–gelatin mixture sample as a function of the azurite content (w/w). The number of incident primary X-ray photons was adjusted, such that the LOD_{Cu} for both the analytical methods were equal (80 ppm). For reference, the azurite concentration of Sample #4 is indicated by a vertical dashed line

painting samples were analyzed. Nevertheless, the radiation dose by PIXRF was still much smaller than that by the conventional XRF for any azurite concentration.

Measurement of the simulated painting samples

Figure 9 shows the PIXRF spectra measured for the test samples with azurite (Sample #4) and smalt (Sample #5) using the Ge and Cu targets. For the sample with azurite, the Cu-KX-ray peaks were clearly visible when the Ge target was used (Fig. 9a). However, no peak was observable when the Cu target was employed, except for the scattered primary X-rays (Fig. 9b). In contrast, for the sample with smalt, the Co-KX-ray peaks were observed both for the spectra obtained using the Ge (Fig. 9c) and Cu (Fig. 9d) targets. The Co-KX-ray yield obtained with the Cu target was higher than that acquired with the Ge target. One reason for this result is that the Cu-KX-ray energy (8.04 keV for K_{α}) as the primary X-ray was nearer to the Co absorption edge (7.71 keV) than the Ge-KX-ray energy (9.87 keV for K_{α}). Another reason is that, as the primary photon, the Cu-KX-ray intensity per incident proton charge (Fig. 3b) was higher than that of the

Ge-KX-rays (Fig. 3a) because of the higher X-ray production cross-section [46]. The results suggest a high element selectivity of the PIXRF analysis.

Figure 10a shows the X-ray spectra measured using the Ge target for the simulated painting sample, where the hemp paper support was painted with azurite and smalt mixture (Sample #6). Ge-KX-rays were used as the primary X-ray; thus, both Cu and Co could undergo K-shell ionization, emitting KX-rays of these elements. The peak intensity of the Co- K_{α} X-ray was much lower than that of the Cu- K_{α} emission simply because of the low Co concentration in smalt. In this case, the overlap of the Cu- K_{α} and Co- K_{α} peaks was not that serious; hence, a quantitative evaluation of the Co peak area was still possible. However, if the Co concentration were a few orders of magnitude lower, the peak area quantification would have been difficult.

Figure 10b depicts the result obtained when the target for the MeV protons was switched to Cu. In this case, except for the scattered primary photons, no Cu-KX-ray peaks appeared because the primary X-ray energy (8.04 keV for Cu- K_{α}) was lower than the K-absorption

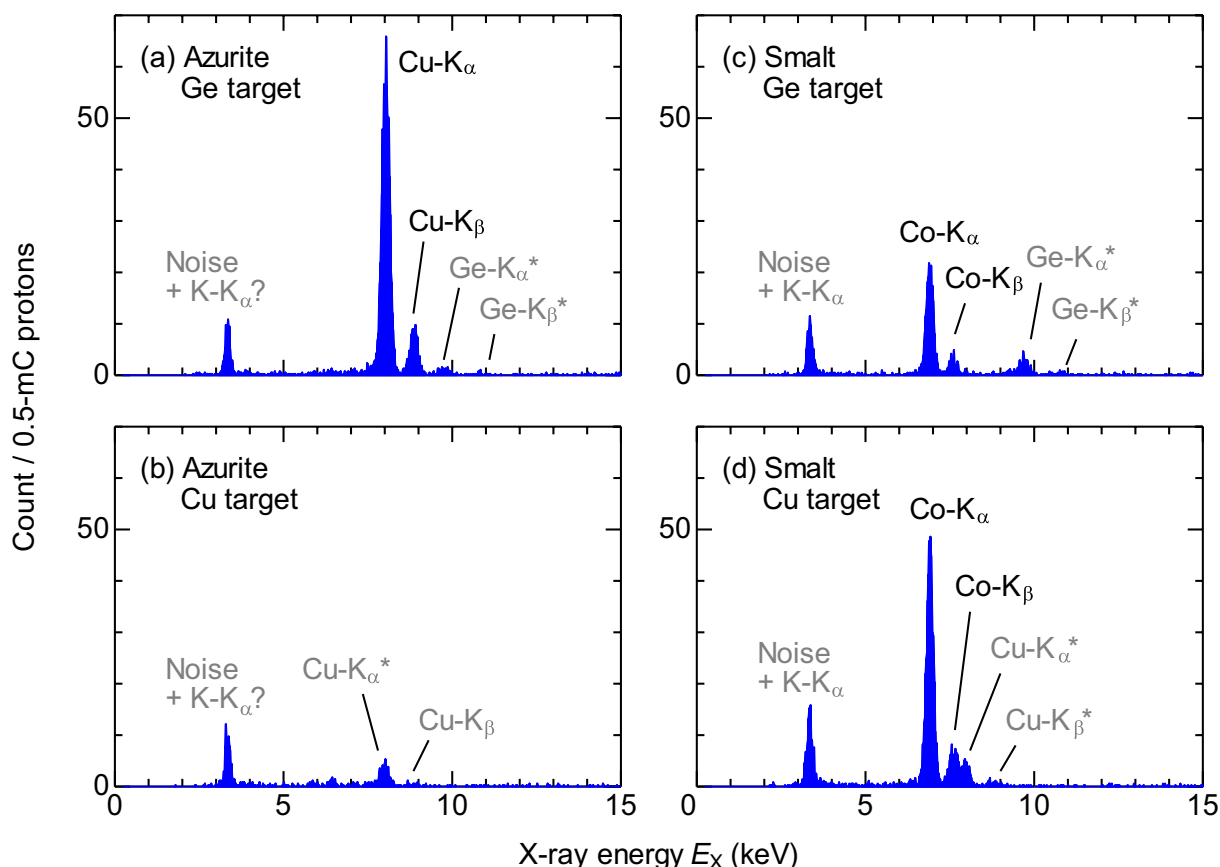


Fig. 9 PIXRF spectra of the simulated samples with azurite (a, b) and smalt (c, d) measured with the Ge and Cu targets. The asterisks (*) indicate the peaks of the scattered primary photons

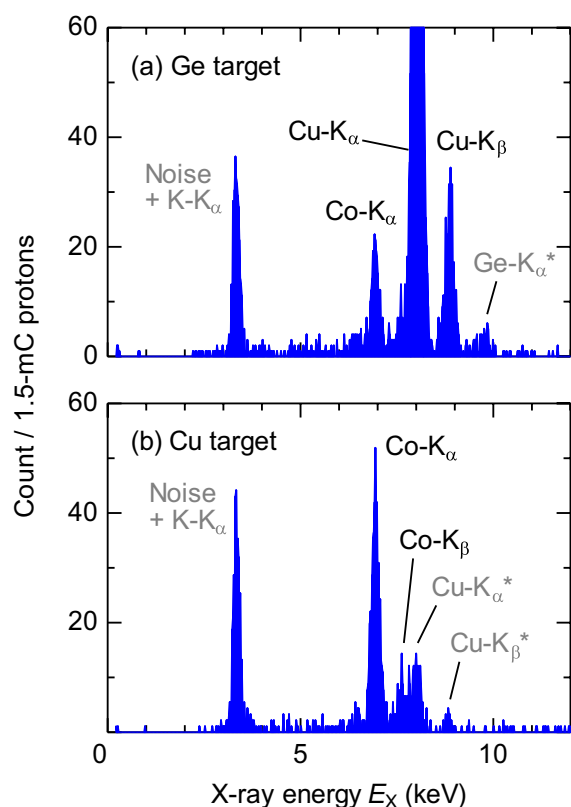


Fig. 10 **a** PIXRF spectra measured using the Ge target for the simulated painting sample, where the hemp paper support was painted with a mixture of azurite and smalt. The height of the Cu- K_{α} X-ray peak was ≈ 200 counts. **b** PIXRF spectrum measured for the same sample with the Cu target. The asterisks (*) indicate the peaks of the scattered primary photons

edge energy of Cu (8.98 keV). The primary X-ray energy was very near the absorption edge of Co (Fig. 3b). Consequently, the Co- K_{α} emission peak was more isolated, and the peak intensity was higher than those in Fig. 10a. This effect was applied to quantify low-concentration platinum ($Z=78$) in gold ($Z=79$) heritage objects [19].

In order to quantify minor element in the sample, the primary X-ray intensity should be increased. In conventional XRF, however, an increase in the power of the primary X-ray beam can cause serious pulse-pile ups due to X-rays from the major element. Comparatively, in PIXRF, we can increase the primary X-ray intensity without causing any serious pulse-pileups. Therefore, even if the peak of the element of interest (in this case Co) does not overlap with the peak of the major element, the suppression of the photon count caused by the major element (in this case Cu) is often advantageous. In addition, the primary X-ray intensity in PIXRF can be increased with less concern regarding the radiation dose received by

the precious sample due to the larger margin for radiation dose to the sample compared to that in conventional XRF.

Conclusions

In this study, we found that PIXRF analysis can potentially provide a low-LOD and -dose performance for the measurement of specific element species. This result can be of help in preventing the possible sensible radiation damage, even as a late effect on the precious historical heritage samples. The experiments using a mixed pigment sample also successfully demonstrated the selective measurement of a minor element mixed with major elements. This can be a powerful tool when the Z -numbers of these elements are near each other.

However, our results do not mean that PIXRF can be used as a substitute for conventional XRF because its advantages are available only for the analysis of particular single element species. In this sense, PIXRF is not anymore considered as a multi-elemental analytical technique. Thus PIXRF cannot be used for completely unknown samples; the samples must be analyzed with other techniques in advance. Such a two-step analysis is time consuming. Moreover, if the first measurement is implemented with a radiation-based technique such as conventional XRF or PIXE, the dose due to the first measurement must also be considered. For example, by simply repeating the same measurement by using the same method, the overall LOD can be reduced to $1/\sqrt{2}$, and the total dose becomes twice of the original value. However, if PIXRF is applied as the second measurement and the overall LOD of a specific element becomes $1/\sqrt{2}$, the total dose can be less than twice of the original value. Nevertheless, to include such a case, the application of PIXRF as the second step should be determined by weighing the cost (increase of measurement time and total dose) versus the benefits (lower overall LOD for the specific element).

The local radiation dose also increases with the increasing Cu concentration, although this occurs also in conventional XRF. The size of the whole system, including a MeV proton accelerator, is much larger than conventional XRF devices like portable ones, although the setup in Fig. 2 is palm sized. Thus, PIXRF could be used as a simple inexpensive supplementary technique to substitute well-established conventional multi-elemental analytical techniques only when we focus on a low-concentration specific element contained in very precious cultural heritage samples. Compatibility with the ordinary PIXE facility would be the best because both methods use MeV proton beams. Although large and/or extremely precious cultural heritage samples cannot be moved from

museums, small and/or less precious artefacts are being routinely moved, for example, to dedicated PIXE facilities [47, 48] at distant locations. Therefore, PIXRF can be used in combination with PIXE analysis for cultural heritage samples.

Note that the selective detection of particular elements through PIXRF cannot be applied to arbitrary element pairs. In this study, we only considered Cu and Co for the selective detection of the element of interest. However, in historical materials, discrimination of element pairs, such as Ca (K-edge at 4.04 keV) and Sb (L_{III} -edge at 4.13 keV); S (K-edge at 2.47 keV) and Pb (M_V -edge at 2.48 keV); and Ti (K-edge at 4.96 keV) and Ba (L_{III} -edge at 5.25 keV), is often difficult owing to spectral overlapping. Among these pairs, the Ca-Sb pair can be separated by using Sc ($E_{K\alpha}=4.09$ keV) as the primary target. In contrast, S-Pb and Ti-Ba pairs cannot be resolved using PIXRF because there exists no appropriate primary target element whose K_{α} -X-ray energy lies between the absorption edges of each pair.

Also, low Z elements, such as Na, Mg, and Al, are often of interest in heritage samples. K-absorption edge energies of Na, Mg, and Al are 1.07, 1.30, and 1.56 keV, respectively. Therefore, the best targets for protons would be Mg ($E_{K\alpha}=1.25$ keV), Al ($E_{K\alpha}=1.49$ keV), and Si ($E_{K\alpha}=1.74$ keV), respectively, which are easily available. However, owing to the low fluorescence yield of these low- Z elements [40], the primary X-ray intensity is insignificant. Therefore, the PIXRF of these low- Z elements is, in principle, expected to not be very effective.

In the present study, typically a 30-min acquisition time was employed for spectral data. The relatively long measurement time was selected due to the low primary proton beam current available in the beam line used. It should be mentioned that other MeV proton accelerator facilities can routinely deliver much higher beam current (1–10 μ A). Provided that higher current beams from such a facility were used, and the primary target was adequately cooled, we could increase the beam current by 10–100 times, dramatically reducing the measurement time.

Among many elements used in pigments, we selected Cu as the sample element in our experiment. Note that Cu is not the only subject of evaluation. In addition, for the experiment, the selection of the sample element species is not very critical because the cross-sections of atomic processes relevant to PIXRF do not change sensitively with the valence state, but change slowly with respect to the atomic numbers of the sample and primary target elements. As a result, the experimentally confirmed low-dose performance for Cu can be extrapolated to other elements.

Abbreviations

ALARA	As Low As Reasonably Achievable
FOM	Figure of Merit
LOD	Limit of Detection
PIN	Positive-Intrinsic-Negative
PIXE	Particle Induced X-ray Emission
PIXRF	Particle Induced X-Ray Fluorescence
XRF	X-Ray Fluorescence

Acknowledgements

The authors thank N. Shiratori for help in operation and management of the experimental facility. We are indebted to H. Kubota for preparation of the X-ray tube. H. Yoshii is gratefully acknowledged for discussion on the radiation dose due to conventional XRF analyses. The Tokyo Tech Green Transformation Initiative (Tokyo Tech GXI) is gratefully acknowledged for financial support in the decommissioning of the accelerator system used for this study.

Author contributions

Research conceptualization: YO, JH; Funding acquisition: YO; Preparation of the experimental setup: YO, JH; Proton accelerator development: HF, NH; Experimental data taking: YO, HF, X-ray spectrum analysis: YO; Radiation dose calculation: JH; Draft writing: YO; Manuscript editing: JH, NH. All authors read and approved the final manuscript.

Funding

This work was supported by JSPS KAKENHI Grant Number 18H00753.

Availability of data and materials

The datasets used and/or analyzed during the current study are available from the corresponding author on reasonable request.

Declarations

Competing interests

The authors declare that they have no competing interests.

Received: 11 November 2022 Accepted: 28 April 2023

Published online: 19 May 2023

References

- Calligaro T, Gonzalez V, Pichon L. PIXE analysis of historical paintings: is the gain worth the risk? *Nucl Instrum Methods B*. 2015;363:135–43. <https://doi.org/10.1016/j.nimb.2015.08.072>.
- Csepregi Á, Szikszai Z, Targowski P, Sylwestrzak M, Müller K, Huszánk R, Angyal A, Dönczö B, Kertész Z, Szarka M, Reiche I. Possible modifications of parchment during ion beam analysis. *Herit Sci*. 2022;10:140. <https://doi.org/10.1186/s40494-022-00781-8>.
- Benzeggouta D, Vickridge I. Handbook on best practice for minimizing beam induced damage during IBA. arxiv. 2004. <https://doi.org/10.48550/arXiv.1303.3171>.
- Mantler M, Klikovits J. Analysis of art objects and other delicate samples: is XRF really nondestructive? *Powd Diffr*. 2004;19:16–9. <https://doi.org/10.1154/1.1649962>.
- Huntley J, Westaway KE, Gore DB, Aubert M, Ross J, Morwood MJ. Non-destructive or noninvasive? the potential effect of X-ray fluorescence spectrometers on luminescence age estimates of archaeological samples. *Geoarchaeology*. 2016;31:592–602. <https://doi.org/10.1002/gea.21574>.
- Mantler M, Schreiner M. X-Ray fluorescence spectrometry in art and archaeology. *X-Ray Spectrom*. 2000;29:3–17. [https://doi.org/10.1002/\(SICI\)1097-4539\(200001/02\)29:1%3c3::AID-XRS398%3e3.0.CO;2-O](https://doi.org/10.1002/(SICI)1097-4539(200001/02)29:1%3c3::AID-XRS398%3e3.0.CO;2-O).
- ICRP. Recommendations of the ICRP, ICRP Publication 26. *Ann ICRP*. 1977;1(3):1–53.
- Mahrok MF, Crumpton D, Francois PE. Proton induced X-ray fluorescence analysis and its application to the measurement of trace elements in hair.

- Nucl Instrum Methods B. 1984;4:120–6. [https://doi.org/10.1016/0168-583X\(84\)90051-X](https://doi.org/10.1016/0168-583X(84)90051-X).
9. Peisach M. Ion beam analytical methods for attempts to establish the provenance of archaeological objects in the absence of reference artefacts. *Nucl Instrum Methods B*. 1986;14:99–115. [https://doi.org/10.1016/0168-583X\(86\)90430-1](https://doi.org/10.1016/0168-583X(86)90430-1).
 10. Saleh NS, Al-Saleh KA. XRF induced by PIXE: Comparison with PIXE. *J Radioanal Nucl Chem Lett*. 1987;108:363–73. <https://doi.org/10.1007/BF02165093>.
 11. Karydas AG, Paradellis T. Proton-induced monochromatic X-ray beams. *X-Ray Spectrom*. 1993;22:252–9. <https://doi.org/10.1002/xrs.1300220415>.
 12. Castiglioni M, Manfredi G, Milazzo M, Silari M. PIXE-induced XRF by high energy protons and alpha particles. *Nucl Instrum Methods B*. 1993;75:38–43. [https://doi.org/10.1016/0168-583X\(93\)95608-8](https://doi.org/10.1016/0168-583X(93)95608-8).
 13. Zeng X, Wu X, Yao H, Yang F, Cahill TA. PIXE-induced XRF with transmission geometry. *Nucl Instrum Methods B*. 1993;75:99–104. [https://doi.org/10.1016/0168-583X\(93\)95620-K](https://doi.org/10.1016/0168-583X(93)95620-K).
 14. Wu X, Zeng X, Yang F. Archaeological applications of PIXE and IXX for paperlike objects at Fudan university. *Nucl Instrum Methods B*. 1993;75:458–62. [https://doi.org/10.1016/0168-583X\(93\)95696-3](https://doi.org/10.1016/0168-583X(93)95696-3).
 15. Silari M, Milazzo M. Conceptual design of a compact photon source in the 1–100 keV range. *Nucl Instrum Methods B*. 1994;89:33–7. [https://doi.org/10.1016/0168-583X\(94\)95140-3](https://doi.org/10.1016/0168-583X(94)95140-3).
 16. Cicardi C, Milazzo M, Manfredi G, Silari M. Feasibility of intense monochromatic x-ray source in the 1–100 keV range by proton bombardment of metallic targets. *X-Ray Spectrom*. 1995;24:45–51. <https://doi.org/10.1002/xrs.1300240205>.
 17. Sokaras D, Zarkadas Ch, Fliegau R, Beckhoff B, Karydas AG. Proton induced quasi-monochromatic x-ray beams for soft x-ray spectroscopy studies and selective x-ray fluorescence analysis. *Rev Sci Instrum*. 2012;83:123102. <https://doi.org/10.1063/1.4768735>.
 18. Lamehi-Rachti M, Oliyai P, Rahighi J, Shokouhi F, Fakhrai M. Application of PIXRF in the analysis of archaeological glazed tiles. *Nucl Instrum Methods B*. 2001;184:430–6. [https://doi.org/10.1016/S0168-583X\(01\)00791-1](https://doi.org/10.1016/S0168-583X(01)00791-1).
 19. Guerra MF, Calligaro T. Gold cultural heritage objects: a review of studies of provenance and manufacturing technologies. *Meas Sci Technol*. 2003;14:1527–37. <https://doi.org/10.1088/0957-0233/14/9/305>.
 20. Guerra MF, Calligaro T. Gold traces to trace gold. *J Archaeol Sci*. 2004;31:199–208. <https://doi.org/10.1016/j.jas.2002.05.001>.
 21. Guerra MF. Fingerprinting ancient gold with proton beams of different energies. *Nucl Instrum Methods B*. 2004;226:185–98. <https://doi.org/10.1016/j.nimb.2004.02.019>.
 22. Uda M, Demortier G, Nakai I. X-rays for archaeology, ISBN 978-1402035807. Dordrecht: Springer; 2005. p. 124.
 23. Mahnke H-E, Denker A, Salomon J. Accelerators and x-rays in cultural heritage investigations. *C R Physique*. 2009;10:660–75. <https://doi.org/10.1016/j.crh.2009.08.003>.
 24. Ploykrachang K, Hasegawa J, Kondo K, Fukuda H, Oguri Y. Development of a micro-XRF system for biological samples based on proton-induced quasimonochromatic X-rays. *Nucl Instrum Methods B*. 2014;331:261–5. <https://doi.org/10.1016/j.nimb.2013.12.043>.
 25. Ploykrachang K, Hasegawa J, Kondo K, Fukuda H, Oguri Y. Design of a proton-induced quasimonochromatic micro-XRF setup for wet biological samples. *Energy Procedia*. 2015;71:252–60. <https://doi.org/10.1016/j.egypro.2014.11.877>.
 26. Coccato A, Moens L, Vandenabeele P. On the stability of mediaeval inorganic pigments: a literature review of the effect of climate, material selection, biological activity, analysis and conservation treatments. *Herit Sci*. 2017;5:12. <https://doi.org/10.1186/s40494-017-0125-6>.
 27. Rapp G. *Archaeomineralogy, natural science in archaeology*, ISBN 978-3540785934. Berlin Heidelberg: Springer; 2009.
 28. Hayakawa Y, Hirao Y, Miura S, Yotsutsuji H, Tokugawa Y. Analysis of the pigment used in the scroll paintings of the tale of Genji, national treasure, by portable X-ray fluorescence spectrometer. *Sci conserv*. 2000;39:1–14.
 29. Hayakawa Y, Hayakawa Y, Miura S, Yotsutsuji H, Tokugawa Y, Nagoya A. Analysis of the painting materials used in the “scroll paintings of the tale of Genji”, national treasure. *Sci conserv*. 2002;41:1–13. <https://doi.org/10.18953/00003581>.
 30. Hayakawa Y. Newly-identified copper-based green-colored pigments and the works they were used for. *Sci conserv*. 2009;48:109–17. <https://doi.org/10.18953/00003745>.
 31. FitzHugh EW, Winter J, Leona M. *Studies using scientific methods: pigments in later Japanese paintings*, freer gallery of art occasional papers. Washington, D.C.: Smithsonian Institution; 2003.
 32. Nagasaki N. “Konjo-biki” painting of Kyoto imperial palace seen from techniques and materials. *Annu Rep Kyoto Off Imp Househ Agency*. 2022;3:70–91.
 33. Sugioka N. Analysis in materials science of the blue colors used for the paintings on room partitions in the seiryu-den Kyoto imperial palace. *Annu Rep Kyoto Off Imp Househ Agency*. 2022;3:92–117.
 34. M4 TORNADO High performance Micro-XRF spectrometer, Bruker Nano GmbH, Berlin, Germany. 2015. <http://donar.messe.de/exhibitor/ounds/2016/T391039/m4-tornado-brochure-eng-439061.pdf>. Accessed 21 Apr 2023.
 35. Belard R, Higuchi H, Perry J, Furunori (aged wheat starch paste): challenges of production in non-traditional settings. *J Inst Conserv*. 2009;32:31–51. <https://doi.org/10.1080/19455220802630735>.
 36. Lee K, Sablier M, Enomae T, Inaba M. Evaluation of degradation of Japanese hanging scrolls using relative peak area of volatile organic compounds. *Stud Conserv*. 2023;68:445–57. <https://doi.org/10.1080/00393630.2022.2049033>.
 37. Newman R. Binders in paintings. *MRS Bull*. 1996;21:24–31. <https://doi.org/10.1557/S0883769400032085>.
 38. Manship E, Cavallo G, Gilardi J, Riccardi MP. Treating smalt: a preliminary SEM-EDX study of the effects of aqueous-based alkaline conservation treatments on smalt in wall paintings. *Stud Conserv*. 2023;68:68–83. <https://doi.org/10.1080/00393630.2021.1940721>.
 39. Hubbell JH, Seltzer SM. *Tables of X-Ray Mass Attenuation Coefficients and Mass Energy-Absorption Coefficients (version 1.4)*. National Institute of Standards and Technology, Gaithersburg, MD; 2004. <https://dx.doi.org/10.18434/T4D01F>. Accessed 27 Oct 2022.
 40. Haschke M, Flock J, Haller M. *X-ray fluorescence spectroscopy for laboratory applications*, ISBN 978-3527344635. Weinheim: Wiley-VCH; 2021.
 41. Energy Dispersive X-ray Fluorescence Spectrometer EDX-8100, Shimadzu Corporation, 2023/First Edition: February 2023. https://www.shimadzu.com/an/sites/shimadzu.com/an/files/pim/pim_document_file/brochures/10371/c142-e049_edx-8100.pdf. Accessed 9 Feb 2023.
 42. DELTA handheld XRF R and D Configuration guide DS_103-09-11, OLYMPUS INNOV-X, 100 Sylvan road, Woburn, MA 01915. 2011. https://gwm-engineering.fi/files/8914/4491/4100/DELTA_XRF_Research_and_Discovery.pdf. Accessed 27 Oct 2022.
 43. Amptek Efficiency Package, Amptek, Inc. <https://www.amptek.com/-/media/ametekamptek/documents/resources/efficiency.zip?dmc=1&la=en&revision=d439ae34-a3da-42b6-91b5-e5f482453f10&hash=7910504660104BDEA7545E085B5ED6D6>. Accessed 18 Oct 2022.
 44. DELTA Family Handheld XRF Analyzer User’s Manual, International edition, 103201-01EN - revision C, Olympus NDT, 48 Woerd avenue, Waltham, 02453 MA, USA. 2012. <https://d272z0j70hk1vf.cloudfront.net/downloads/5876bf18afc10-103201-01en-rev-c1-delta-family-user-international.pdf>. Accessed 27 Oct 2022.
 45. Lechtman E, Pignol JP. Interplay between the gold nanoparticle sub-cellular localization, size, and the photon energy for radiosensitization. *Sci Rep*. 2017;7:13268. <https://doi.org/10.1038/s41598-017-13736-y>.
 46. Lapicki G. Cross sections for K-shell X-ray production by hydrogen and helium ions in elements from beryllium to uranium. *J Phys Chem Ref Data*. 1989;18:111–218. <https://doi.org/10.1063/1.555838>.
 47. Salomon J, Dran J-C, Guillou T, Moignard B, Pichon L, Walter P, Mathis F. Ion-beam analysis for cultural heritage on the AGLAE facility: impact of PIXE/RBS combination. *Appl Phys A*. 2008;92:43–50. <https://doi.org/10.1007/s00339-008-4512-4>.
 48. Calusi S. The external ion microbeam of the LABEC laboratory in Florence: some applications to cultural heritage. *Microsc Microanal*. 2011;17:661–6. <https://doi.org/10.1017/S1431927611000092>.

Publisher’s Note

Springer Nature remains neutral with regard to jurisdictional claims in published maps and institutional affiliations.